INTERNATIONAL JOURNAL FOR NUMERICAL METHODS IN FLUIDS, VOL. 25, 567–598 (1997)

A NUMERICAL INVESTIGATION OF 2D, STEADY FREE SURFACE FLOWS

G. D. TZABIRAS*

Heroon Polytechniou 9, Zografos 157 73, Athens, Greece

SUMMARY

Systematic tests have been performed to study the behaviour of a numerical method developed to calculate 2D, steady free surface flows. The Reynolds equations are solved in the physical space by employing a non-orthogonal staggered grid, while the k–ε model is adopted to approximate the Reynolds stresses. The free surface is calculated following an iterative procedure and various parameters that affect convergence and accuracy of the numerical solution have been examined. Calculated results are compared with measured data for two cases, i.e. the wave generation above a bottom topography at various Froude numbers and the free surface formation above a submerged hydrofoil. © 1997 by John Wiley & Sons, Ltd.

Int. J. Numer. Meth. Fluids, **25**: 567–598 (1997).

No. of Figures: 34. No. of Tables: 6. No. of References: 31.

KEY WORDS: free surface flows; finite volumes; k–ε model

1. INTRODUCTION

The calculation of 2D, steady free surface flows has received particular interest in applications of computational fluid dynamics. Apart from representing real problems, e.g. many cases in open channel hydraulics,[1] these flows are offered for evaluating 3D numerical methods. Although such methods have recently been applied with success in marine hydrodynamics to calculate the wave generation around ships,[2] the determination of the free surface by solving the Navier–Stokes equations requires excessive computer power. This is why they have been applied so far only to simple hull forms at model scale. A common practice to investigate their performance with respect to accuracy and convergence is to test these methods in 2D applications.

Depending on the examined problem, potential or viscous flow methods can be applied to calculate 2D flows with a free surface. Potential solutions may be categorized in two general groups, i.e. the boundary element approaches and those that solve the discretized Euler equations. The former have been proved the most effective for obtaining quick solutions[3–5] and therefore for performing parametric studies.[6] Euler methods have been applied mostly to solve flow fields around submerged hydrofoils,[7–9] while some of them have been developed to study the performance of advanced numerical techniques, e.g. the unstructured grid approximation.[8]

When viscous phenomena are dominant, the Navier–Stokes or the Reynolds equations have to be solved numerically to obtain realistic results. Unfortunately, the computing demands of relevant

---

* Correspondence to: G. D. Tzabiras, Department of Naval Architecture and Marine Engineering, National Technical University of Athens, Heroon Polytechniou 9, Zografos 157 73, Athens, Greece

CCC 0271–2091/97/050567–32 $17.50

Received July 1996

methods are significantly higher than those of applying potential flow solvers. Most of the viscous flow codes developed so far treat the free surface problem as time-dependent, i.e. the steady solution is reached through a physically consistent iterative procedure.[10–13] More or less, the main effort in these methods has been focused on acquiring solutions, while systematic studies concerning the influence of characteristic parameters on the convergence behaviour are rather limited. In some cases[11] the effect of the grid size on the numerical solution has been examined, but without obtaining nearly grid-independent results. Lungu and Mori[12] have performed remarkable tests regarding the effect of discretization schemes, boundary conditions and higher-order, Eulerian free surface approximations on flow calculations about a hydrofoil, but their applications were restricted to laminar flow cases and they have not been compared with experimental data. However, it must be noted that, even with their improved techniques, convergence to steady state was achieved in almost 30,000 time steps, which is a rather slow rate.

An alternative way to achieve steady state solutions is to apply iterative methods that solve successively the steady Navier–Stokes equations. In this case the problem becomes the determination of a free boundary that satisfies the necessary conditions, without taking into account time derivatives in intermediate steps. Such procedures may be advantageous, since they neglect memory effects that preserve oscillating trends which decelerate convergence. In this sense the scope of the present work is to study the behaviour of a steady state procedure when various 2D problems are examined, i.e. free surface flows about bottom topographies and submerged hydrofoils. An effort is made to investigate how some crucial numerical and physical parameters affect the numerical solution as well as to compare computational with experimental results.

3. NUMERICAL METHOD

2.1. Governing equations

It is assumed that the Reynolds and the continuity equations describe the incompressible and turbulent free surface flow around the two-dimensional bodies that are examined. To calculate the Reynolds stresses which appear in the momentum equations, the isotropic eddy viscosity k–ε model[14] is employed, i.e. two more differential equations are introduced to close the system of unknown variables. In a Cartesian co-ordinate system (x_1, x_2) any transport equation can be written in the general form

$$\rho\frac{\partial\Phi}{\partial t}+\rho\frac{\partial u_1\Phi}{\partial x_1}+\rho\frac{\partial u_2\Phi}{\partial x_2}=\frac{\partial}{\partial x_1}\left(\Gamma_\Phi\frac{\partial\Phi}{\partial x_1}\right)+\frac{\partial}{\partial x_2}\left(\Gamma_\Phi\frac{\partial\Phi}{\partial x_2}\right)+S_\Phi, \tag{1}$$

where ρ is the fluid density, (u_1, u_2) are the mean velocity components corresponding to (x_1, x_2) and Φ denotes a scalar variable. The left-hand side (LHS) of (1) includes the partial derivative of Φ with respect to time t and the convection of Φ by the mean flow. The first two terms on the right-hand side (RHS) of (1) stand for the diffusion of Φ, while the source term S_Φ depends on the examined variable and its expressions are presented in Table I together with those of the diffusion coefficient Γ_Φ.

In Table I, μ denotes the molecular viscosity of the fluid, while μ_t is the turbulent (or eddy) viscosity which, according to the standard k–ε model, is calculated as

$$\mu_t=\rho C_\mu k^2/\varepsilon, \tag{2}$$

where $C_\mu = 0{\cdot}09$, k is the turbulence kinetic energy and ε is its dissipation rate.

Table I. Source terms of transport equations

ϕ	Γ_ϕ	S_ϕ
u_1	$\mu_e = \mu + \mu_t$	$-\frac{\partial p^*}{\partial x_1} + \frac{\partial}{\partial x_1}\left(\mu_e \frac{\partial u_1}{\partial x_1}\right) + \frac{\partial}{\partial x_2}\left(\mu_e \frac{\partial u_2}{\partial x_1}\right)$
u_2	$\mu_e = \mu + \mu_t$	$-\frac{\partial p^*}{\partial x_2} + \frac{\partial}{\partial x_1}\left(\mu_e \frac{\partial u_1}{\partial x_2}\right) + \frac{\partial}{\partial x_2}\left(\mu_e \frac{\partial u_2}{\partial x_2}\right)$
k	$\mu + \mu_t$	$G - \rho\varepsilon$, where $G = 2\mu_t\left[\left(\frac{\partial u_1}{\partial x_1}\right)^2 + \left(\frac{\partial u_2}{\partial x_2}\right)^2 + \frac{1}{2}\left(\frac{\partial u_1}{\partial x_2} + \frac{\partial u_2}{\partial x_1}\right)^2\right]$
ε	$\mu + \mu_t/1{\cdot}3$	$1{\cdot}44G\frac{\varepsilon}{k} - 1{\cdot}92\rho\frac{\varepsilon^2}{k}$

The variable p^* in the source term of the two momentum equation is equal to the sum of the static pressure p and the gravitational body force, i.e.

$$p^* = p + \rho g h, \tag{3}$$

where g is the gravitational acceleration and h denotes the vertical distance from a reference level.

The finite volume method is applied to solve numerically the system of transport equations (1). The calculation domain is covered by a non- orthogonal, body-fitted H-mesh having one set of co-ordinate lines always parallel to the Cartesian axis x_2 (Figure 1). Since the free surface is transformed during the solution procedure, this type of grid presents the advantage of quick and simple adjustment. Besides, it is beneficial for obtaining efficient expressions with regard to convergence as well as for calculating accurately the grid velocities when the problem is treated as time-dependent. However, one should note that this mesh is not always suitable for describing complex underwater geometries. In such cases, effective solutions can be obtained either by applying domain decomposition techniques or by introducing unstructured grid methodologies.[8,11,12]

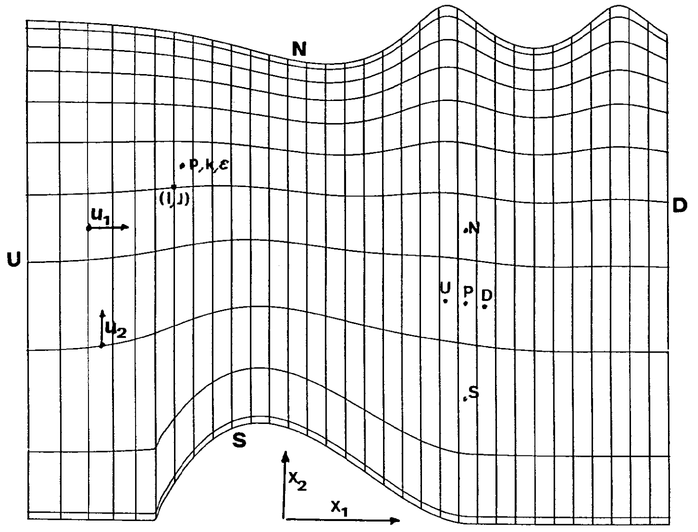

Figure 1. Non-orthogonal mesh above bottom topography

A staggered grid arrangement is adopted to solve the strongly coupled momentum and continuity equations, i.e. the velocity components are defined at different points from the pressure which is calculated at the centre of cell (I, J) (Figure 1). Each transport equation is integrated in the corresponding control volume and results in a discretized equation of the general form

$$A_{\mathrm{P}}\Phi_{\mathrm{P}} = A_{\mathrm{N}}\Phi_{\mathrm{N}} + A_{\mathrm{S}}\Phi_{\mathrm{S}} + A_{\mathrm{D}}\Phi_{\mathrm{D}} + A_{\mathrm{U}}\Phi_{\mathrm{U}} + S_{\Phi I}, \tag{4}$$

where N, S, D and U correspond to the neighbouring points of the central node P in the physical space. Equation (4) is derived by applying central differences in space to approximate the partial derivatives of Φ. In the x_2-direction these derivatives can be expressed directly through the values at the respective grid points, whereas parallel to the x_1-axis they are implicitly calculated from the gradient

$$\frac{\partial\Phi}{\partial s} \approx \frac{\partial\Phi}{\partial x_1}\frac{\delta x_1}{\delta s} + \frac{\partial\Phi}{\partial x_2}\frac{\delta x_2}{\delta s}. \tag{5}$$

The partial derivative on the LHS of (5) is explicitly calculated from the values at the grid points along the curvilinear s-direction, while δx_1 and δx_2 represent the projections of the distance δs (between successive nodes) on the co-ordinate axes x_1 and x_2 respectively.

The coefficients A_i, $i = $ N, S, D, U, in (4) represent the combined effect of the convection and diffusion terms appearing in the transport equation (1). Diffusion terms can always be approximated by central differences without causing any convergence problems.[15] In the x_1-direction they include only the first term on the RHS of (5), while the second term is integrated as a source term. To obtain unconditionally convergent solutions, the convective part of A_i is approximated by first-order upstream or central differences so that A_i is always positive. The application of this lower-order scheme requires fine grids to reduce numerical diffusion errors, unless the grid lines are aligned with the flow lines. To overcome this shortcoming as far as possible, the x_1-grid lines are continuously transformed to streamlines during the solution procedure. This is accomplished by calculating the streamfunction values at grid points through the integrals

$$\Psi(x_1, h_2) = \int_{h_1}^{h_2} u_1(x_1, x_2)\mathrm{d}x_2 + \Psi(x_1, h_1) \tag{6}$$

and then interpolating the initial Ψ-values on the inlet boundary U of the computational domain (Figure 1). The limits within which a streamlined grid is formed depend on the problem being examined. If a body lies within the domain, as in the case of a hydrofoil beneath a free surface, then the streamfunction is not monotone near stagnation or any separation region and the method cannot produce lines that are functions of x_1. In such cases the aforementioned procedure is applied outside a zone surrounding the body, denoted by SL in Figure 2, while an exponential distribution is used for the grid points up to the solid boundary.

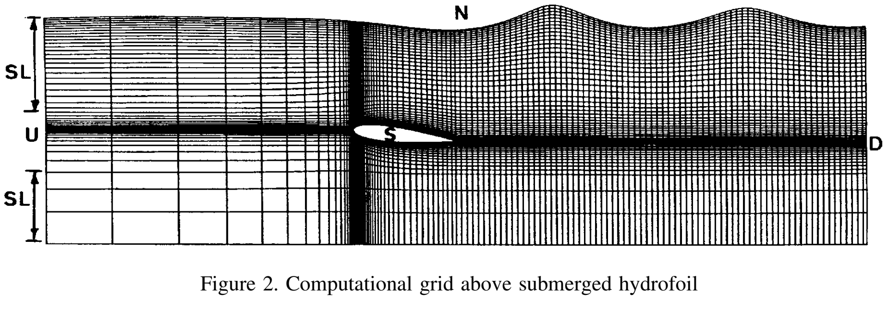

Figure 2. Computational grid above submerged hydrofoil

The solutions of the steady state problems which are examined in the present study can be obtained either by following successive steady steps or by applying a time-dependent procedure. Evidently in the former case the time derivative on the LHS of (1) is omitted, while it has to be evaluated when the problem is treated as time-dependent. However, as the mesh varies continuously, this evaluation cannot be performed using the standard Eulerian approximation; instead, it is necessary to apply the concept of moving grids.[16,17] When the differential transport equations are integrated in finite volumes, the integral of $\partial\Phi/\partial t$ is approximated following the first-order Reynolds transport theorem:[18]

$$\frac{\partial}{\partial t}\int_V \Phi \mathrm{d}v \approx \int_{V(t+\delta t)} \frac{\partial\Phi}{\partial t}\mathrm{d}v + \int_{S(t)} \Phi_S(t)\vec{u}_g \mathrm{d}\vec{s}, \tag{7}$$

where $V(t)$ denotes the control volume at time t, $V(t+\delta t)$ denotes the control volume at time $t+\delta t$, Φ_S is the boundary value on the surrounding surface S of $V(t)$, $\vec{u}_g$ is the velocity of points on S due to the transformation of the grid and $\mathrm{d}\vec{s}$ is the normal vector to S. According to the mean value theorem, the LHS of (7) can be approximated as

$$\frac{\partial}{\partial t}\int_V \Phi \mathrm{d}v \approx \frac{\displaystyle\int_{V(t+\delta t)} \Phi(t+\delta t)\mathrm{d}v - \int_{V(t)} \Phi(t)\mathrm{d}v}{\delta t} \approx \Phi_P \frac{V(t+\delta t)}{\delta t} - \Phi_O \frac{V(t)}{\delta t}, \tag{8}$$

where Φ_P is the value at the centre of control volume $V(t+\delta t)$ and Φ_O is the corresponding value for $V(t)$. In cases where the grid varies simultaneously in all directions, there are difficulties in defining the grid velocities, so space conservation laws must be adopted to approximate the corresponding integrals.[16,17] However, when the grid changes only in one direction, as in the case under consideration, the surface integral of (7) can be directly evaluated via the mean value theorem as

$$\int_{S(t)} \Phi_S(t)\vec{u}_g \mathrm{d}\vec{s} \approx \Phi_n(t)\delta x_1 u_{gn} - \Phi_s(t)\delta x_1 u_{gs}, \tag{9}$$

where δx_1 is the length of the control volume along the x_1-axis, Φ_n and Φ_s stand for the mean values on the upper (north) and lower (south) sides of $V(t)$ respectively and u_{gn} and u_{gs} are the corresponding grid velocities. For a straight line segment it is easy to show that the latter can be calculated through the abscissae of the middle pooints of the north and south sides as

$$u_{gn} = x_{2n}(t+\delta t) - x_{2n}(t), \qquad u_{gs} = x_{2s}(t+\delta t) - x_{2s}(t). \tag{10}$$

Introducing (8) and (9) in (7), the integration of the time derivative at $t+\delta t$ is approximated as

$$\int_{V+\delta V} \frac{\partial\Phi}{\partial t}\mathrm{d}v \approx \Phi_P \frac{V(t+\delta t)}{\delta t} - \Phi_O \frac{V(t)}{\delta t} - \Phi_n(t)\delta x_1 u_{gn} + \Phi_s(t)\delta x_1 u_{gs}. \tag{11}$$

The first term on the RHS of (11) can be included in the main coefficient A_P of the discretized equation (4), which becomes

$$A_P = \sum_i A_i + \rho \frac{V(t+\delta t)}{\delta t}. \tag{12}$$

The remaining terms of (11) are included in the source term $S_{\Phi t}$. This treatment corresponds to a first-order implicit time-marching scheme, since all other variables in (4) are evaluated at $t+\delta t$. Obviously the preceding analysis refers to the solution of time-dependent flows. However, many methods neglect the terms of (11) which involve the grid velocities when steady state problems are examined. Apparently this simplification is allowed because the time derivative vanishes when the solution converges.

2.2. *Boundary conditions*

The numerical solution of the elliptic-in-space, discretized equations (4) requires the specification of boundary conditions on each boundary of the calculation domain of Figure 1. On the upstream line U the u_1- and u_2-velocity components as well as the turbulence characteristics have known values that characterize the problem under consideration, i.e. Dirichlet conditions are introduced.

On the solid surface boundary S the wall function method[14] is employed to calculate the wall shear stress and the turbulence quantities. It is assumed that the non-dimensional velocity u^+ follows the logarithmic distribution

$$u^+ = \begin{cases} y^+ & \text{for } y^+ < 11{\cdot}63, \\ (1/\kappa)\ln(Ey^+) & \text{for } y^+ \geqslant 11{\cdot}63, \end{cases} \tag{13}$$

where

$$u^+ = \frac{u_P}{\sqrt{(\tau_w/\rho)}}, \qquad y^+ = \sqrt{(\tau_w/\rho)}\frac{y_R}{\nu},$$

$\kappa = 0{\cdot}42$, $E = 9{\cdot}79$, τ_w is the wall shear stress, y_R is the normal distance from the solid boundary and u_P is the velocity component parallel to the wall. Under the assumption that in the near-wall region the production of turbulence kinetic energy equals its dissipation rate, the following expression can be derived for the wall shear stress:

$$\tau_w = f_w u_P, \tag{14}$$

with

$$f_w = \begin{cases} \mu/y_R & \text{for } y^+ < 11{\cdot}63, \\ \rho C_\mu^{0{\cdot}25}\sqrt{k}\kappa/\ln(Ey^+) & \text{for } y^+ \geqslant 11{\cdot}63. \end{cases}$$

Supposing that u_P coincides with the local velocity vector (one-dimensional Couette flow), the integrated result $f_w\delta s_1$ of the wall shear stress in the x_1-direction is added to the coefficient A_P of the adjacent-to-the-wall component $u_1(I, 2)$ (Figure 3). In addition, the corresponding coefficient A_S is set equal to zero, since the convection term on the wall vanishes. For non-orthogonal staggered grids the calculation of convection and diffusion terms on the south face BC of the control volume of the near-wall component $u_2(I, 3)$ needs special treatment. The values of u_2 and its x_2-derivatives on BC cannot be approximated adequately using linear relations when BC lies in a fully turbulent zone. To calculate the necessary quantities, it is assumed that the total convection C_s through BC is equal to the difference of the integrals

$$C_s = \rho\left(\int u_1 \mathrm{d}x_2\right)_D^C - \rho\left(\int u_1 \mathrm{d}x_2\right)_A^B, \tag{15}$$

which are evaluated by applying the velocity distribution law (13) in the normal direction. The value of u_{2s} at the centre of BC, which appears in the discretized form of the $u_2(I, 3)$ momentum equation, is obtained by approximating C_s as

$$C_s = \rho u_{2s}(x_{1C} - x_{1B}) - 0{\cdot}5\rho[u_1(I+1, 2) + u_1(I, 2)](x_{2C} - x_{2B}). \tag{16}$$

Then the combined effect of viscous stresses on BC is calculated by applying the integrated form of the u_2-momentum to the cell ABCD of Figure 3, which corresponds to the grid point on the wall where $u_1 = u_2 = 0$. Evidently, to retain conservation, this effect is equal to the viscous force which acts on the south face of the $u_2(I, 3)$ control volume. In the aforementioned equation the wall effect appears as the projection along x_2 of the τ_w shear force which is implicitly introduced to calculate the total force on BC. The calculated values of u_1 and u_2 on this line are used to calculate the integrated generation and dissipation terms of the k-equation according to the classical wall function method,[14] while the sum of the convection and diffusion terms on the solid boundary is set equal to zero, i.e. $A_S = 0$ on AD. Finally, the value of ε at the centre P of the adjacent-to-the-wall cell is computed using a simplified mixing length distribution[14] as

$$\varepsilon = \frac{C_\mu^{0\cdot75} k^{1\cdot5}}{\kappa y_R}, \tag{17}$$

which is a Dirichlet condition on the ε-equation. As described in the sequel, the pressure correction method which is followed calculates the pressure values up to the same point P. Assuming that close to the solid boundary the normal pressure gradient equals zero, the values of pressure p^* at points P are accordingly extrapolated on the wall. Then they are used to calculate p_w on the middle of sides AD (Figure 3) by linear interpolation. The values of p_w appear in the source terms of the discretized momentum equations.

Following the majority of relevant numerical studies, the free surface contour N is not considered as an interface boundary between two fluids with different densities, but as a free boundary on which the following two basic conditions are valid.

(a) The sum of the normal stresses on N equals the external pressure p_o (ambient pressure), while the shear stress and the surface tension are neglected (dynamic boundary condition).
(b) Since in the steady state problem the free surface represents a flow line, the normal velocity component or, equivalently, the total convection on N is equal to zero (kinematic boundary condition). The kinematic boundary condition has to be fulfilled at the end of the solution procedure, because the geometry of the free surface is not *a priori* known.

If it is assumed that $p_o = 0$, then the dynamic boundary condition results as

$$p_N^* = \rho g h, \tag{18}$$

which specifies pressure values at the free surface points that influence the corresponding momentum equations. The N-boundary staggered control volumes of u_1 and u_2, corresponding to line I in the x_1-direction, are sketched as $A_2B_1C_1D_2$ and $A_3B_3C_3D_3$ respectively in Figure 4. If NJ denotes grid points on N, the component $u_1(I, NJ-1)$ is calculated at A_3 and $u_2(I, NJ)$ at C_1. In several methods the value $u_1(I, NJ)$ at B_3 is approximated by linear extrapolation and a Neumann condition is applied on N, while u_2 is calculated by the continuity equation which demands certain assumptions for the local pressure distribution. However, there is no restriction on calculating the values of both u_1 and u_2 on N through the solution of the discretized momentum equations. In this case it can be easily shown that the coefficient A_N of (4) becomes identically equal to zero for cells (I, NJ), i.e. a Neumann

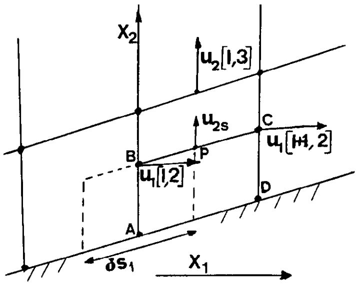

Figure 3. Control volumes in wall region

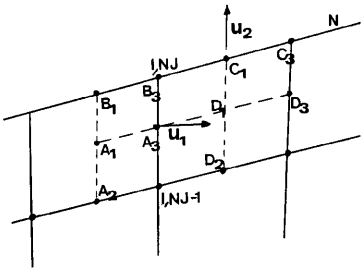

Figure 4. Control volumes at free surface

condition is applied to both momentum equations, while the $u_1(I, NJ)$ control volume $A_1B_1C_1D_1$ is a part of the control volume $A_2B_1C_1D_2$. Evidently this approach, which is followed in the present applications, does not require additional assumptions on the free surface. In any case the k–ε equations are solved up to $NJ - 1$ points and the Neumann condition $A_N = 0$ for cells $(I, NJ - 1)$ is applied.

Owing to the absence of information about the flow variables on the downstream boundary D, simplifying assumptions have to be adopted. The basic approximation being followed is that the pressure values on D are extrapolated from preceding nodes. If NI denotes the last grid points on D (Figure 5), the values $p^*(NI, J)$ are calculated by applying the first-order Taylor expansion

$$p^*(NI, J) = p^*(NI - 1, J) + \frac{\partial p^*}{\partial x_1}\delta x_1 + \frac{\partial p^*}{\partial x_2}\delta x_2. \tag{19}$$

The partial derivative $\partial p^*/\partial x_2$ is calculated by central differences on line $NI - 1$, while $\partial p^*/\partial x_1$ is calculated implicitly by applying (19) on lines $NI - 2$ and $NI - 1$. Assuming also that the normal derivative on D of the stress σ_{11} is equal to zero (fully developed flow), the u_1-momentum can be solved up to line NI by simply setting $A_D = 0$ for cells (NI, J) in (4). Consequently, the u_1-component is calculated on D just as on any other line of the calculation domain. It should be noted that the values $u_1(NI, J)$ appear in the integrated form of the continuity equation which is used to compute the pressure field. On the same boundary it is assumed that the normal derivatives of all other variables vanish, i.e. the Neumann condition $\partial\Phi/\partial x_1 = 0$, $\Phi = u_2$, k, ε is applied.

The application of the aforementioned procedure for calculating the boundary values of u_1 and p^* on D is similar to the non- reflecting boundary conditions which have been applied with success in strongly recirculating flows past 2D bodies.[19,20] The basic concept in this approximation is that instead of extrapolating values of the velocity on the downstream boundary, which is the usual practice in many works,[21] it is better to extrapolate terms that exist in the corresponding momentum equation.

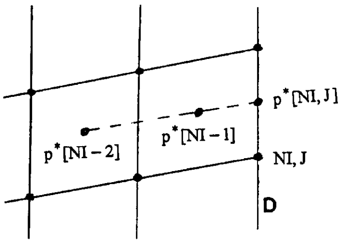

Figure 5. Control volumes at downstream boundary

2.3. Solution procedure

The steps of the iterative algorithm followed to obtain convergence to steady state are described in Table II. In the first external iteration $K = 1$ a guess for the velocity components, the pressure field and the turbulence quantities is initially made, whereas the free boundary N is assumed to be a horizontal line that coincides with the undisturbed water level. The velocity u_1 is set equal to U_o, i.e. the velocity at infinity that characterizes the examined problem, while the values of all other variables are set equal to zero. Apparently $p^* = 0$ implies that the reference level for the hydrostatic pressure is the undisturbed free surface. Then the solution follows steps 2–4 which solve successively the momentum, the pressure correction and the turbulence model equations. The pressure correction equation follows in general the principles of the SIMPLE[22] algorithm as described in the next subsection. For a specified boundary N the aforementioned procedure is applied *Nmax* times, where *Nmax* has a predetermined value. For $K = 1$ the computations are continued until convergence is achieved in order to obtain a numerically correct approximation, i.e. the *Nmax* limit is applied for $K > 1$. To achieve convergence in any case, the application of underrelaxation factors is necessary. If Φ_S denotes the solution of system (4) for any transport variable, the updated value Φ_n to be used in subsequent operations is calculated as

$$\Phi_n = r\Phi_o + (1 - r)\Phi_S, \qquad (20)$$

where r is the underrelaxation factor and Φ_o is the value of the variable calculated in the previous step. The introduction of underrelaxation is made according to Reference 23, i.e. equation (20) is applied to the initial coefficients of the discretized system (4) as

$$A'_P = A_P/r, \qquad S'_{\Phi I} = S_{\Phi I} + (1 - r)A'_P\Phi_o. \qquad (21)$$

In the following the underrelaxation factors for the velocity components, the pressure and the turbulence characteristics will be referred to as *ru*, *rp* and *rv* respectively. After step 5 in Table II a new free surface is calculated (step 6) and steps 1–6 are repeated until convergence is achieved, i.e. the kinematic condition is fulfilled.

In the Lagrangian sense the exact kinematic condition correlates the velocity components with the positions that a free surface particle follows in time. If $h(x_1, t)$ describes free surface points, this relation is expressed as

$$u_1 = \frac{dx_1}{dt} = \frac{x_1(t + dt) - x_1(t)}{dt}, \qquad u_2 = \frac{dx_2}{dt} = \frac{h(x_1 + dx_1, t + dt) - h(x_1, t)}{dt}. \qquad (22)$$

Theoretically, application of (22) should predict accurately the motion of the free surface provided that the velocity components are known functions of space and time. However, in discretized systems, various approximations of (22) are introduced depending on the numerical scheme and the problem being considered. In the adopted co-ordinate system the fulfilment of the kinematic

Table II. Convergence procedure

Step	
1	Iteration $K = 1$: initial guess for field variables
2	Solution of u_1- and u_2-momentum equations
3	Solution of pressure correction equation; update velocity and pressure
4	Solution of turbulence model equations; update effective viscosity
5	Repeat steps 2–4 *Nmax* times
6	Calculation of new free surface $h(x_1)$
7	$K = K + 1$: repeat steps 2–6 until convergence

condition at the end of a convergence procedure means that the convection term which appears in the discretized form of the continuity equation vanishes on the free surface (Figure 6):

$$C_n = u_{2M}\delta x_1 - u_{1M}[h(x_1 + \delta x_1, t) - h(x_1, t)] = 0, \tag{23}$$

where $u_{1M} = 0{\cdot}5[u_1(I, NJ) + u_1(I+1, NJ)]$ and $u_{2M} = u_2(I, NJ)$ denote the velocity components at the middle M of the line segment between nodes (I, NJ) and $(I+1, NJ)$, corresponding to fixed x_1-values. In this respect, two methods have been tested to calculate successive free surface changes.

The first method follows the Lagrangian formulation (22) and calculates the new free surface elevation at point $I+1$ or $x_1 + \delta x_1$ according to

$$h(x_1 + \delta x_1, t + \delta t) = h(x_1 + \delta x_1') + \frac{u_{2M}}{u_{1M}}(\delta x_1 - \delta x_1'). \tag{24}$$

The distance $\delta x_1'$ in (24) is calculated to satisfy $\delta x_1 - \delta x_1' = u_{1M}\delta t$ according to the first of definitions (22). Assuming that for an adequate grid discretization in x_1 the free boundary can be approximated as a straight line segment between x_1 and $x_1 + \delta x_1$, any convergence procedure $h(t + \delta t) \rightarrow h(t)$ results in

$$\frac{h(x_1 + \delta x_1) - h(x_1 + \delta x_1')}{\delta x_1 - \delta x_1'} = \frac{h(x_1 + \delta x_1) - h(x_1)}{\delta x_1} = \frac{u_{2M}}{u_{1M}}, \tag{25}$$

which is equivalent to the discretized condition (23). Relation (24) has been used whenever the final solution is obtained through a sequence of steady problems. In these cases the time step δt appears only in the computation of $\delta x_1'$ and acts as a geometric underrelaxation factor. To assure that $\delta x_1 > \delta x_1'$ always, the value of the time step is selected to be less than

$$\delta t_m = rt \min(\delta x_1 / u_{1M}) \tag{26}$$

among all segments on the free surface. In (26), rt stands for the underrelaxation factor of the time step.

The second method which is examined to approximate the new free surface elevation is based on a truncated form of the exact definitions (22). Using first-order Taylor expansions for $h(x_1 + \delta x_1, t + \delta t)$ and $x_1(t + \delta t)$, one may obtain

$$u_2 \approx \frac{(\partial h/\partial t)\delta t + (\partial h/\partial x_1)\delta x_1}{\delta t} \quad \text{or} \quad \frac{\delta h(x_1, t)}{\delta t} \approx \frac{\partial h(x_1, t)}{\partial x_1} u_1 - u_2. \tag{27}$$

Relation (27) is often referred to as the Eulerian approximation of the free surface, since corresponding changes are predicted only in the vertical direction x_2, i.e. for constant x_1- values. Owing to this advantage, it has been widely used in marine hydrodynamics and particularly in 3D applications around complex configurations. Theoretically there is no restriction on applying (27) to both steady and unsteady problems, while its accuracy depends on the selection of the time step. If it

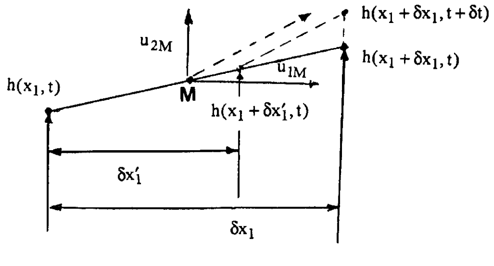

Figure 6. Determination of new free surface elevation

is applied at the middle M of the surface segment defined by δx_1, then, to be compatible with (23) at the end of the iterative procedure, it is apparent that the first derivative of the free boundary, $\partial h/\partial x_1$, should be set equal to $[h(x_1 + \delta x_1) - h(x_1)]/\delta x_1$. Since the free surface elevation is computed at M, an interpolation method is needed to compute the values of $h(x_1)$ and $h(x_1 + \delta x_1)$. The classical cubic spline interpolation has been adopted in this work.

2.4. Pressure correction equation

As already mentioned, the pressure field is calculated according to a correction method which is associated with the staggered grid employed. Supposing that (u_1, u_2) represents a solution of the momentum equations, there is a need to correlate the velocity changes δu_1 and δu_2 with the corresponding pressure correction gradients $\delta p'$ so that ($u_1 + \delta u_1$, $u_2 + \delta u_2$) satisfies the integrated continuity equation in the pressure control volume. In the classical SIMPLE[22] approach this is accomplished by assuming

$$\delta u_1 = Du_1 \delta p'_1, \qquad \delta u_2 = Du_2 \delta p'_2, \tag{28}$$

where Du_1 and Du_2 are functions of the field variables and are calculated from the integrated form of the momentum equations (4) as

$$Du_1 = \frac{V_{u_1}}{\delta x_1 A p_{u_1}}, \qquad Du_2 = \frac{V_{u_2}}{\delta x_2 A p_{u_2}}. \tag{29}$$

In (29), V_u is equal to the cell area of the corresponding velocity component, δx is the distance along the Cartesian axes between successive pressure nodes and A_P is calculated after (12). Apart from the simplifications which are inherent in expressions (28), their application to non-orthogonal grids requires further approximations which influence drastically the convergence of the velocity and pressure fields. For the adopted grid system the first approximation is related to the linking of the velocity change δu_1 with the pressure gradient δp_1 along the x_1-axis. Since the grid is non-orthogonal in this direction, pressure forces act on every face of the u_1-momentum control volume. On the north as well as on the south side of this volume they are calculated by interpolating pressure values. Therefore there is not a simple way to obtain an expression like the first of (28) and δp_1 is approximated using pressure values at successive nodes, while Du_1 is calculated after (29). A second simplification is related to the u_1-fluxes through the north and south faces of the pressure control volume, which are also calculated using linear interpolations. Although these fluxes are included in the calculation of the total mass balance S_M, there are not explicit formulae to correlate the corresponding velocity changes with pressure gradients. To avoid ill-conditioned matrices for the pressure correction p' if terms like the aforementioned are included, the latter are omitted and application of relations (28) leads to the equation

$$A_P p'_P = A_N p'_N + A_S p'_S + A_D p'_D + A_U p'_U + S_M, \tag{30}$$

with $A_P = \sum A_i$, $i =$ N, S, D, U. Equation (30) is similar to the general discretized equation (4), both being solved by successive applications of the TDMA[24] algorithm. The source term S_M is equal to the sum of the mass fluxes through the faces of the pressure control volume and vanishes when the field variables converge. With the specified boundary conditions for the velocity components, Neumann (zero-gradient) conditions should be applied for the pressure correction on boundaries U, D and S, while the Dirichlet condition $p' = 0$ holds on the free surface where the pressure is known. Despite the approximations which have been applied, one should keep in mind that the pressure correction equation has no physical meaning and is introduced to attain convergence of the momentum and continuity equations. However, depending on the skewness of the cells, these approximations may influence convergence quite unfavourably. In order to improve the convergence rate with the adopted non-orthogonal mesh, three modifications have been examined.

First, a more accurate expression has been applied to couple the velocity with the pressure changes. Apparently relations (28) imply that the terms which take into account the influence of neighbouring points on the RHS (4) have been neglected. Assuming that the pressure gradients do not vary significantly between control volumes with common faces, we may obtain the recursive formula[25]

$$Du^{(n)} = Du^{(o)} + \sum_i A'_i Du_i^{(n-1)}. \tag{31}$$

The first term on the RHS of (31) is expressed as in (29), while the second term represents the influence of adjacent points. The coefficients A'_i are functions of both the geometry and the corresponding finite volume coefficients of (4). The number (n) denotes the order of approximation. For upstream schemes it has been found that sufficient values of (n) may be lower than four. Adoption of (31) in 2D and 3D applications has been proved very advantageous.[25,26] Actually, the corresponding coefficients in the pressure correction equation are intensified, allowing for higher pressure underrelaxation factors. Besides, they are associated with the momentum equations in a more rigorous way. Apparently approximation (31) can be applied to either orthogonal or non-orthogonal grids.

The second improvement is related to the change in u_1-fluxes on the north and south sides of the pressure control volume (Figure 7). Supposing again that the pressure gradient along x_1 does not change significantly in the vertical direction, a change in the u_1-flux C'_n on the north face may be related to $\delta p'$ according to

$$C'_n = 0{\cdot}5\rho[Du_{nu}(p'_U - p'_P) + Du_{nd}(p'_P - p'_D)](x_{2nu} - x_{2nd}), \tag{32}$$

where the coefficients Du are calculated by linear interpolation among the corresponding values in the x_2-direction. Evidently the sign of C'_n depends on the sign of the projected distance $Ex_2 = x_{2nu} - x_{2nd}$. To retain only positive terms in the formation of the finite volume coefficients, expression (32) is transformed to changes in the coefficient A_U or A_D as follows:

$$\begin{aligned} \delta A_D &= 0{\cdot}5\rho(Du_{nu} + Du_{nd}/f_d)\max(0, Ex_2), \\ \delta A_U &= 0{\cdot}5\rho(Du_{nu} + Du_{nd}f_d)\max(0, -Ex_2). \end{aligned} \tag{33}$$

The above relations have been derived under the assumption that the pressure varies linearly along x_1, which is involved through the factor $f_d = [x_1(I+2) - x_1(I)]/[x_1(I+1) - x_1(I-1)]$. Similar approximations can be derived on the south side of the pressure cell.

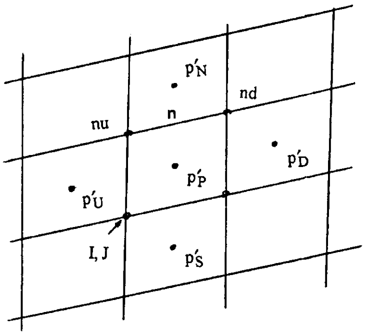

Figure 7. Pressure control volume

The last modification has been the application of a multiple solution of system (30). If this system is solved once, the velocities corrected after (28) will not in general satisfy the continuity equation, because the source term S_M includes non-orthogonal fluxes. It is reasonable to recalculate this term using the updated velocity components and solve the system again. This procedure can be repeated several times until the mass sources vanish, but one must consider the associated increase in CPU time, since the pressure solution is the most time-consuming. The final pressure correction equals the algebraic sum of the intermediate changes, while the coefficients A_i in (30) have to be calculated once.

The effect of the aforementioned modifications has been studied in the case of unbounded turbulent flow around an NACA 0012 hydrofoil section. The tested incidence angle was 8° and the Reynolds number $7{\cdot}5\times10^5$. A grid of $NI\times NJ=500\times100$ grid points has been used, where NI denotes grid points along x_1 and NJ along x_2. Uniform velocity conditions were imposed on the upstream, north and south boundaries of the rectangular computational domain. Most computations were carried out using the underrelaxation factors $ru=0{\cdot}6$ (velocity), $rp=0{\cdot}3$ (pressure) and $rv=0{\cdot}4$ (k and ε). Figure 8 shows the influence of various parameters on the convergence rate. The horizontal axis shows the number of iterations (steps 2–4, Table II), while the vertical axis represents the non-dimensional total residual, i.e. the sum of the corresponding residuals of the momentum and continuity equations. The residual of any transport equation is calculated as the sum of the absolute differences between the two sides of the discretized form (4), i.e.

$$Res(\Phi)=\sum_N\left|A_P\Phi_P-\sum_i A_i\Phi_i-S_{\Phi I}\right|,\tag{34}$$

where N is the total number of computational points. The non- dimensional residual for the momentum equations is calculated if expression (34) is divided by ρHU_o^2, U_o being the velocity at infinity and H the height of the calculation domain at the upstream boundary. The corresponding residual for the continuity equation is equal to the sum of the absolute values of the mass sources S_M in (30), non-dimensionalized by ρHU_o. The number IP in the legend of Figure 8 stands for the TDMA iterations performed to solve the pressure correction equation (30). Whenever a multiple solution is applied, this is denoted as the product of the number of additional solutions and the number of TDMA iterations. The number IR is equal to the order (n) of the recursive formula (31), while $IC=1$ denotes the application of (33) to improve the shortcomings of non-orthogonality.

It noticeable that with the adopted underrelaxation factors, convergence could not be achieved with the classical SIMPLE method, i.e. for $IP=15$, $IR=0$ and $IC=0$. In contrast, by applying any of the above modifications, the solution converged at rates depending on the relevant factors. Generally the differences among the tested cases are not significant, while with $IP=3\times15$, $IR=2$ and $IC=1$ the best convergence rate was achieved. A total of 1790 iterations were required to obtain a total residual less than 10^{-3}, which was a sufficient criterion for convergence of the lift and drag coefficients. The case $IP=15$, $IR=2$, $IC=1$ shows the same stable behaviour as the aforementioned, while the required iterations increased to 1910. Quite similar trends are observed for $IP=15$, $IR=2$ and $IC=0$, except that an instability appears around 400 iterations which, depending on the conditions, may be intensified. The case with $IR=0$ presented the lowest convergence rate and required 2350 iterations to satisfy the aforementioned criterion, implying that the pressure underrelaxation is a crucial parameter.

Basically, the main advantage of the adopted approaches is related to the high underrelaxation factors which can be applied without causing convergence problems. The influence of underrelaxation is presented in Figure 9, where the first three cases correspond to $IP=15$, $IR=2$ and $IC=1$. As observed, the use of a higher underrelaxation factor for the pressure, $rp=0{\cdot}8$, shows an increasing trend in the number of iterations necessary to obtain convergence, which was found equal

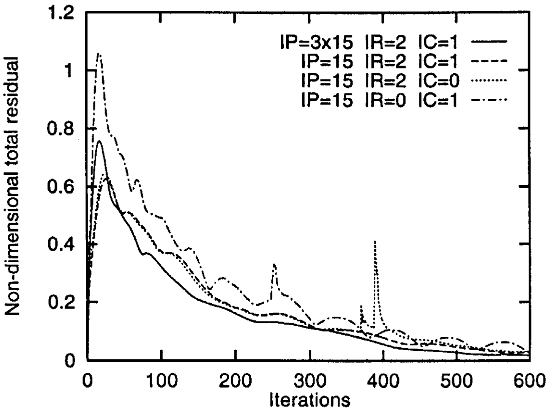

Figure 8. Influence of various approximations on convergence rate

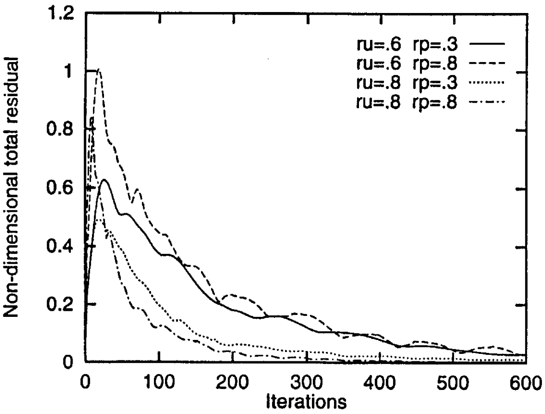

Figure 9. Influence of underrelaxation factors on convergence rate

to 2083. In contrast, higher underrelaxation for the velocity components, $ru = 0{\cdot}8$, improved the convergence rate drastically and required 1210 iterations. The best behaviour was obtained for $ru = rp = 0{\cdot}8$, but this case converged with $IP = 3 \times 15$ and $IR = 4$, i.e. the computing cost per iteration was higher. However, the number of iterations reduced drastically to 730. In all cases the underrelaxation factor for the turbulence characteristics was kept constant, i.e. $rv = 0{\cdot}6$.

3. TEST CASES

3.1. Bottom topography

The first test case was the calculation of the wave generation above the experimental profile of Cahouet,[3] for which experimental data have been provided at various Froude numbers. The geometry of the profile, which was placed on the bottom of a recirculating water tunnel, is described by the equation

$$y = \frac{27}{4}\frac{E}{l^3}x(x - l)^2, \tag{35}$$

where $E = 0{\cdot}042$ m denotes the maximum height y of the profile, $l = 0{\cdot}42$ m denotes its length and x is the distance from the leading point. The Froude number of the flow is defined through the fluid velocity U_o far upstream and the undisturbed water depth h as

$$Fr = U_o/\sqrt{(gh)}. \tag{36}$$

In all experimental cases, measurements of the velocity distribution upstream of the profile revealed that the flow was fully turbulent. Therefore no transition area was taken into account in the calculations. Three characteristic cases have been selected for comparison, corresponding to a supercritical, a subcritical and a critical Froude number. The kinematic viscosity of the water was assumed always equal to 10^{-6} m^2 s^{-1}.

Computations were first performed for the supercritical Froude number $Fr = 2{\cdot}05$. The still water depth was $h = 0{\cdot}09545$ m and the upstream velocity $U_o = 1{\cdot}985$ m s^{-1}. A grid of $NI \times NJ = 400 \times 30$ nodes was used to calculate the viscous flow, extending from $-0{\cdot}5$ to $1{\cdot}0$ m, where, as in all relevant applications, the point $x_1 = 0$ coincides with the leading point of the bottom topography. The height of the first grid cells adjacent to the wall was constant along x_1 and equal to $0{\cdot}003$ m, resulting in non-dimensional y^+-values between 90 and 110, i.e. around the upper limit of the suggested range for applying wall functions, which is roughly 30–100. The height of the first free surface cell on the upstream boundary U was equal to $0{\cdot}002$ m, while the other grid points on the same boundary were distributed exponentially up to the middle of the water depth, starting from either the bottom or the free surface. This specification of the first line nodes, followed for all tested Froude numbers, allows the clustering of mesh points in regions where rapid changes in the flow variables exist, i.e. close to the free and solid boundaries. In this particular supercritical case, which was the easiest to obtain grid-independent results for, the same principle was applied to specify grid nodes on each constant x_1-line, the depth being defined as the difference between the free surface height h and the bottom line.

Calculations for the supercritical case presented a significantly higher convergence rate than any other application. This behaviour has also been observed in 3D computations past ship models.[27] The convergence history, solving the problem by successive steady steps and following the Lagrangian free surface correction (24), is shown in Figure 10, where two curves are plotted. The full curve corresponds to the normalized sum of the absolute changes in the free surface (f.s.) elevations on the vertical grid lines:

$$\text{normalized sum of f.s. changes} = \frac{\sum_{NI} |h_i^{(K)} - h_i^{(K-1)}|}{\sum_{NI} |h_i^{(2)} - h_i^{(1)}|}, \tag{37}$$

where K denotes the iteration step for a specified free surface boundary and the denominator is equal to the corresponding sum at $K = 2$. The latter is usually close to the maximum sum. The broken lines in Figure 10 represents the normalized sum of the absolute values of the convection terms C_n (23), on the free boundary, defined as follows:

$$\text{normalized sum of convection terms on f.s.} = \frac{\sum_{NI} |C_n^{(K)}|}{\sum_{NI} |C_n^{(1)}|}. \tag{38}$$

It is interesting that the two curves practically coincide, implying, as expected, that geometrical convergence assures fulfilment of the kinematic boundary condition. However, the sum of the convection terms (38) has been considered more effective for comparisons with different grid sizes, because it represents a flow quantity which is not influenced significantly by the node arrangement, while (37) depends on the number as well as on the concentration of grid points. Figure 10 shows that convergence has been achieved in 700 iterations (or steps). In each K-iteration, 10 internal calculation steps were performed for solving the momentum, pressure correction and turbulence model equations. The corresponding underrelaxation factors were $ru = 0{\cdot}7$, $rp = 0{\cdot}5$ and $rv = 0{\cdot}5$, while for the time step (26) the value $rt = 0{\cdot}9$ was adopted. During the iterative procedure the free boundary moves like a wave which decays downstream, as shown in Figure 11, where X and Y stand for the horizontal and the vertical axis respectively. The calculated wave profile after convergence is close to the measure one (Figure 12). According to Cahouet,[3] all relevant figures include the uncertainty interval of measurements. In the supercritical case the free surface follows the profile contour, whereas the height of the observed wave was predicted equal to 0·045 m, i.e. within the experimental uncertainty interval of about $0{\cdot}046 \pm 0{\cdot}003$ m.

Next the subcritical Froude number was examined. Experiments were carried out for a nominal still water depth $h = 0{\cdot}21$ m and an upstream fluid velocity $U_0 = 0{\cdot}6171$ m s^{-1}, corresponding to $Fr = 0{\cdot}43$. This test case exhibits special interest because a stable, repetitive wave pattern was generated above the topography, being suitable for numerical grid dependence tests. A 500×60 grid was first applied to study the effect of some characteristic parameters. The computational domain extended from $x_1 = -1$ to 1 m. The heights of the adjacent-to-the-wall cells were equal to 0·003 m, resulting in y^+-values ranging between 30 and 70, while the height on the boundary U of the first free surface cell was equal to 0·001 m. The latter ensured that at the end of the computations at least 15 grid points were located within a wave height. Comparative tests were initially made by solving the steady equations and following the Lagrangian free surface correction (24). Ten internal steps were used for each iteration with specified free boundary. The adopted underrelaxation factors were $ru = 0{\cdot}6$, $rp = 0{\cdot}5$ and $rv = 0{\cdot}6$, the order of the recursive formula (31) was $IR = 2$ and corrections (33) were applied in the pressure correction equation ($IC = 1$). The underrelaxation factor rt, defined through (26), was found to be the most crucial parameter that affected the convergence rate. Figure 13 shows the convergence history for two different rt-values, i.e. 0·2 and 0·5. Apparently the higher $rt = 0{\cdot}5$ requires a significantly lower number of iterations to obtain convergence, being almost half of the corresponding number with $rt = 0{\cdot}2$. Then, using $rt = 0{\cdot}5$, the effect of the multiple solution of the pressure equation was examined. Comparing the two cases with $IP = 15$ and 3×15 in Figure 14, it may be concluded that the number of pressure solver iterations is not of crucial importance in this particular problem.

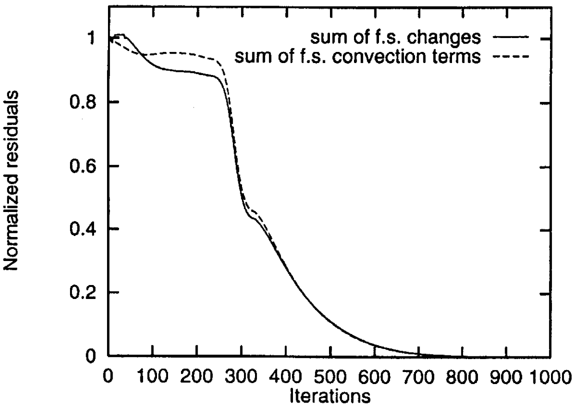

Figure 10. Convergence rates of normalized free surface residuals

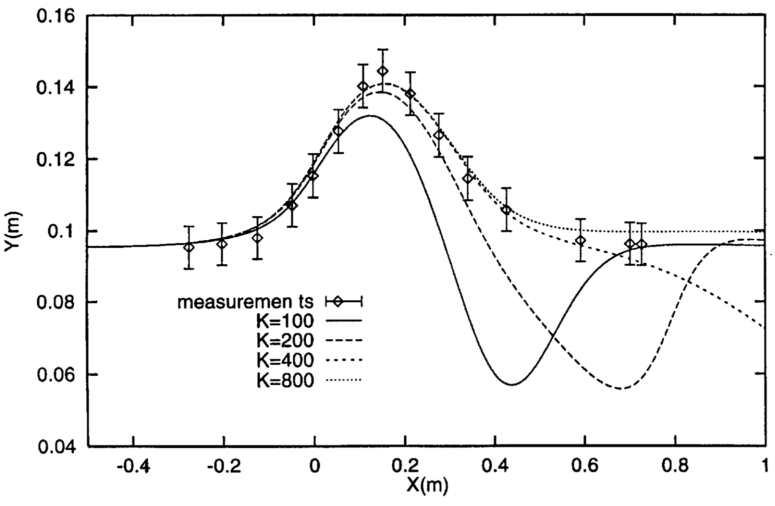

Figure 11. Free surface boundary at different iteration steps K

The influence of the grid structure on the numerical solution is shown in Figure 15, where the free surface contour has been calculated using two different grid generators, i.e. the aforementioned exponential and a streamlined grid created above $0{\cdot}3h$ by interpolating the streamfunction values (6). Although the convergence behaviour was found similar in the two cases, it is clear that the streamlined grid predicted more accurately the measured wave pattern, owing to the more efficient approximation of the convective terms. Similar trends were observed when a finer (750×60) grid was applied. The effect of the downstream boundary conditions on the calculated free surface contour is shown in Figure 16, where the results obtained using the exponential grid and the non-reflecting boundary conditions (described in Section 2.2) are compared with linear extrapolations for all flow variables. A difference in both the wave amplitude and the wavelength is observed between the two solutions. It is remarkable that, owing to incompressibility as well as the two-dimensional character

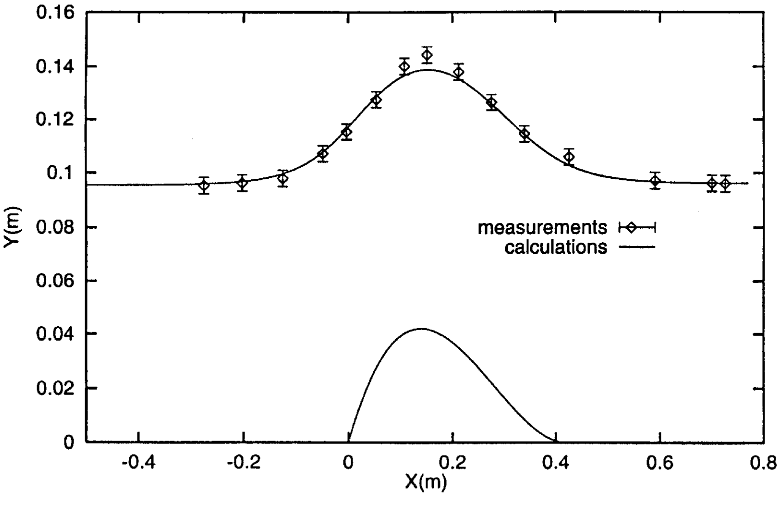

Figure 12. Calculated and measured wave pattern at $Fr = 2{\cdot}05$

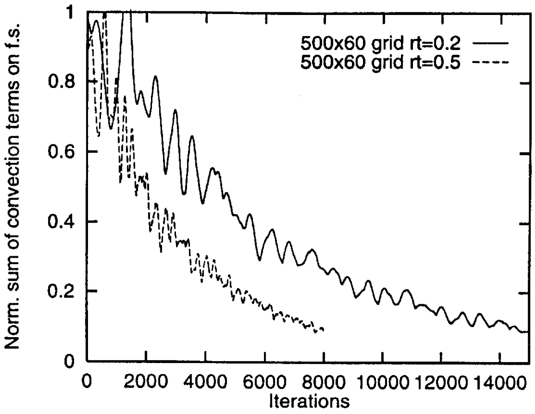

Figure 13. Convergence rates using different time underrelaxation factors

of the flow, the downstream conditions influence the numerical results considerably upstream. With the non-reflecting boundary conditions the calculated first and second wavelengths were noticeably constant and equal to 0·240 m, while the wave amplitudes after the first crest were equal to 0·0154, 0·0154 and 0·0140 m respectively. The corresponding wavelengths calculated with the simplified conditions were equal to 0·240 and 0·231 m, i.e. they tend to reduce close to the downstream boundary. Besides, in the latter computations the wave amplitudes were calculated as 0·0180, 0·0150 and 0·0122 m, showing a rapid decay which is inconsistent with the experimental data.

Using the same grid and convergence parameters, the behaviour of the numerical solution of the time-dependent equations was examined. Since in this case the successive solution in time steps represents a real (and not a quasi-steady) problem, the free surface calculation should follow the laws that govern the fluid motion. Therefore the Eulerian first-order surface approximation (27) has been used in all relevant calculations. To study the differences between the two solutions due to time derivatives, relation (27) was also applied in the steady state procedure. Figure 17 compares the two convergence rates. Evidently the steady solution converges considerably faster than the time-dependent case, implying that the time derivatives introduce memory effects that preserve fluctuations. However, similar applications using finer grids have shown that these effects tend to

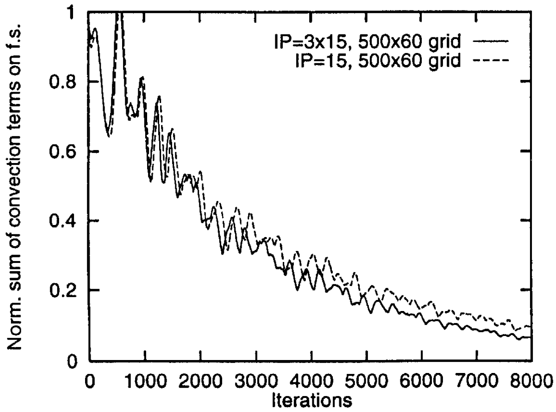

Figure 14. Convergence rates using different pressure solution iterations

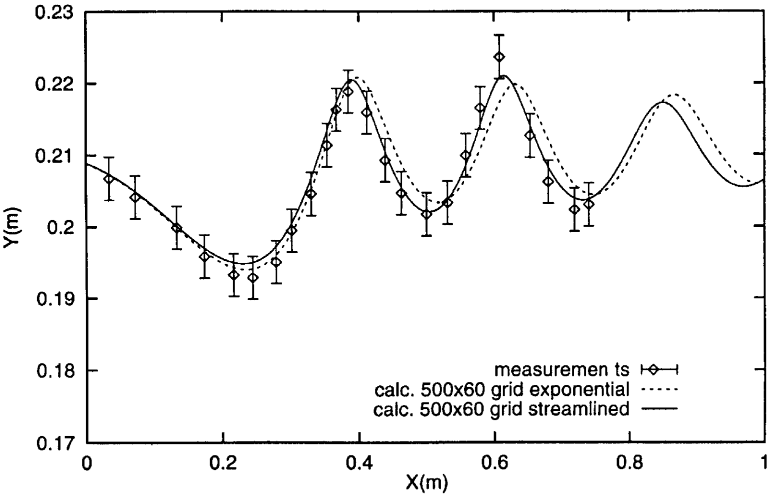

Figure 15. Influence of grid structure on numerical solution

reduce. Comparing also Figures 13 and 17, it is observed that the Eulerian free surface correction leads to faster convergence than the application of the Lagrangian relation (24). Similar behaviour has been observed in other applications,[12] where higher-order Eulerian schemes appear superior with respect to Lagrangian approximations. However, the application of (27) on the middle points M of the free surface segments (Figure 6) required significantly higher longitudinal grid resolutions to produce the same wave contours as those predicted by applying (24). Owing to this performance, which is rather related to the spline approximation for defining grid points through midpoint elevations, the Lagrangian approximation has been used in all steady computation procedures.

Grid dependence tests at the subcritical Froude number have also been performed in order to study the influence of the longitudinal mesh refinement on the calculated results. Three cases were

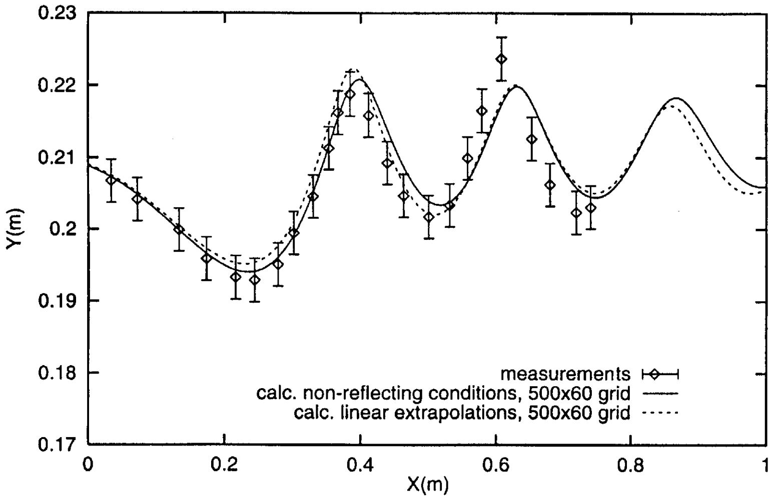

Figure 16. Influence of downstream boundary conditions on numerical solution

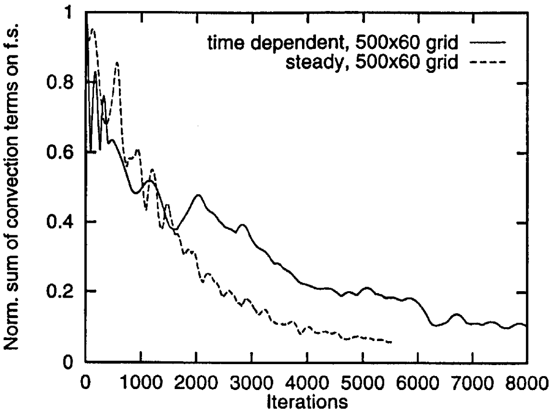

Figure 17. Comparison of convergence rates between steady and time-dependent procedures

examined, corresponding to 550 × 60, 750 × 60 and 950 × 60 grid points. In all of them the computational domain extended from $x_1 = -1$ to 1 m. The underrelaxation factors were $ru = 0{\cdot}8$, $rp = 0{\cdot}7$, $rv = 0{\cdot}7$ and $rt = 0{\cdot}5$, while for the pressure correction equation the parameters $IP = 3 \times 15$, $IR = 2$ and $IC = 1$ were adopted. To investigate the effect of grid refinement on the wave formation, 150 points were used in all cases along x_1, varying exponentially from $x_1 = -1$ to 0 m, while grid nodes after $x_1 = 0$ where equally spaced. A streamlined grid was generated above $0{\cdot}3h$ and the steady iterative method was followed. The convergence rates with the three meshes are plotted in Figure 18, showing that the numerical solution converges drastically faster as the grid becomes coarser. This behaviour is related to the time step underrelaxation factor which, according to (26), is proportional to the node spacing and therefore is reduced on finer grids. Nevertheless, the trends of the convergence history indicate that it would be more effective to solve the problem by using successively refined meshes, as described by Farmer *et al.*[21] for 3D calculations past ships. The predicted wave contours plotted in Figure 19 show that the calculated free surface profiles are in good agreement with the measured ones and almost coincide up to the third wave trough for all tested grids. Significant differences are observed only along the last wavelength, where the finer grid preserves the wave amplitude while the coarser one shows a rapid decay. The calculated results for the wave amplitude $2A$ (crest to trough) and the wavelength obtained with the finest mesh are compared with the measured data in Table III. In this table the 'numerical uncertainty' has been derived by calculating the deviation of the calculated results during the last steps of the solution procedure. Since the numerical solution presents a converging but also oscillating behaviour, the computations stopped when this deviation became lower than the presented bounds. These bounds have been reached in 8000, 14,000 and 25,000 iterations for the grids of 550 × 60, 750 × 60 and 950 × 60 nodes respectively, while the corresponding residual (36) was about 8×10^{-2} in each case. Taking into account the uncertainty intervals, the calculated values in Table III show generally a satisfactory agreement with the experimental data. The calculated free surface boundary at different iterative steps K is presented in Figure 20, while a general view of the generated wave above the bottom topography is shown in Figure 21.

The critical Froude number $Fr = 0{\cdot}52$ exhibits particular interest because experiments showed that small upstream disturbances caused instabilities that destroyed the initially generated steady wave pattern. The still water depth h was equal to 0·28 m and the upstream velocity U_0 equal to 0·862 m s^{-1}. Two sets of computations were first carried out to study the differences between the steady and time-dependent calculation procedures. The calculation domain extended from $x_1 = -1$ to

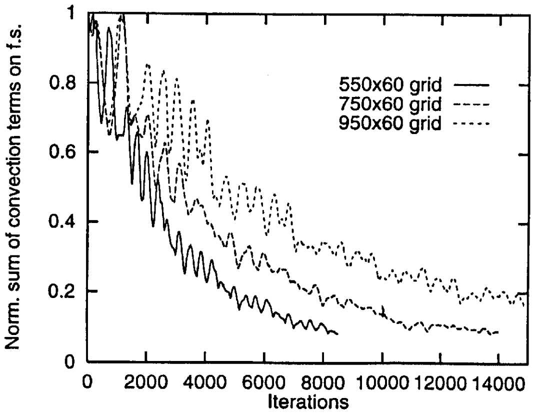

Figure 18. Convergence rates using different grid densities

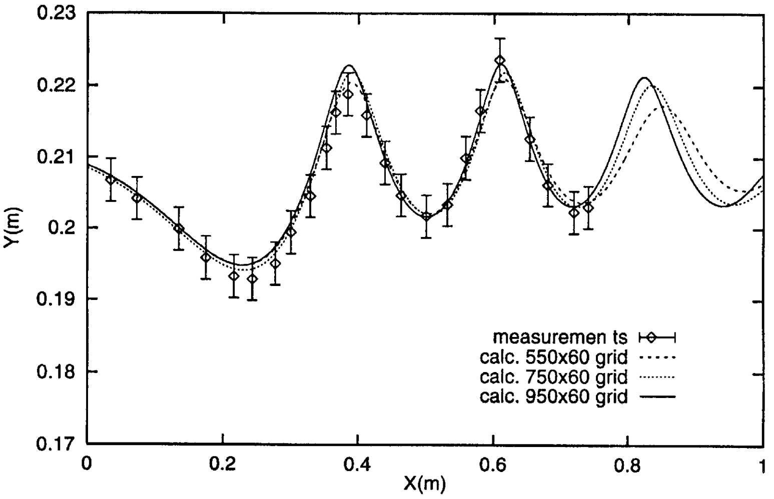

Figure 19. Grid dependence tests and comparison with measurements at $Fr = 0{\cdot}43$

1·60 m, the heights of the first near-wall cells were equal to 0·003 m, the height of the upstream free surface cell was equal to 0·002 m and a 750×60 grid was applied. In both cases the same underrelaxation factors were used, i.e. $ru = 0{\cdot}7$, $rp = 0{\cdot}7$, $rv = 0{\cdot}6$ and $rt = 0{\cdot}5$. The free surface geometry was calculated following the Eulerian approximation (27) and the parameters $IP = 2 \times 15$, $IR = 2$ and $IC = 1$ were adopted to solve the pressure correction equation. The convergence histories of the steady and time-dependent solutions are plotted in Figure 22. It is important that the steady

Table III. Comparison between calculated and measured wave characteristics for $Fr = 0{\cdot}43$

	Wavelength (m)	First wave amplitude 2*A* (m)	Second wave amplitude 2*A* (m)
Measured	0·23 ± 0·02	0·022 ± 0·004	0·019 ± 0·003
Calculated	0·22 ± 0·01	0·028 ± 0·002	0·021 ± 0·001

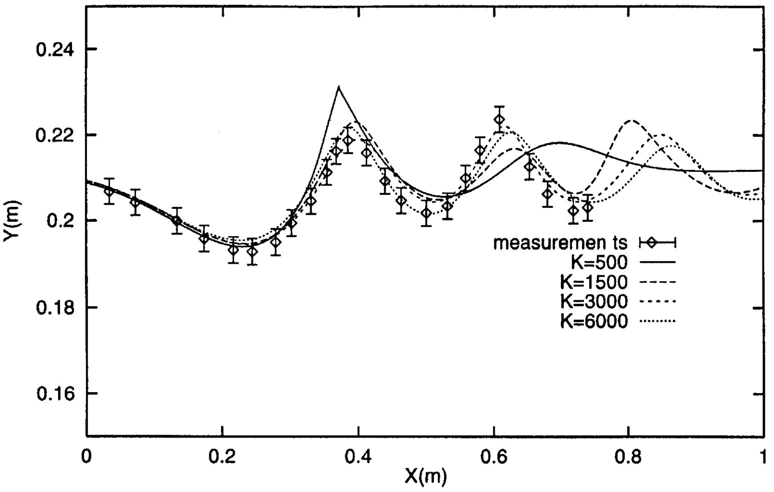

Figure 20. Free surface boundary at different iteration steps K

state algorithm converges in almost 10,000 iterations, while even after this number the time-dependent solution shows continuous fluctuations. If the solution beneath the still water surface ($K = 1$), which has no physical evidence, could be considered as an arbitrary initial numerical disturbance, then the aforementioned trends seem to be consistent with the instabilities which were observed during experiments.

Next, keeping the same convergence parameters as previously, steady computations were performed using two grids of 750×60 nodes, i.e. an exponential grid and one streamlined above $h = 0{\cdot}3$. In both cases convergence was achieved in 13,000 iterations and the calculated wave profiles are compared with the measured free surface elevations in Figure 23. Apparently the two grids predict almost the same wave pattern, showing that at the examined Froude number and the particular

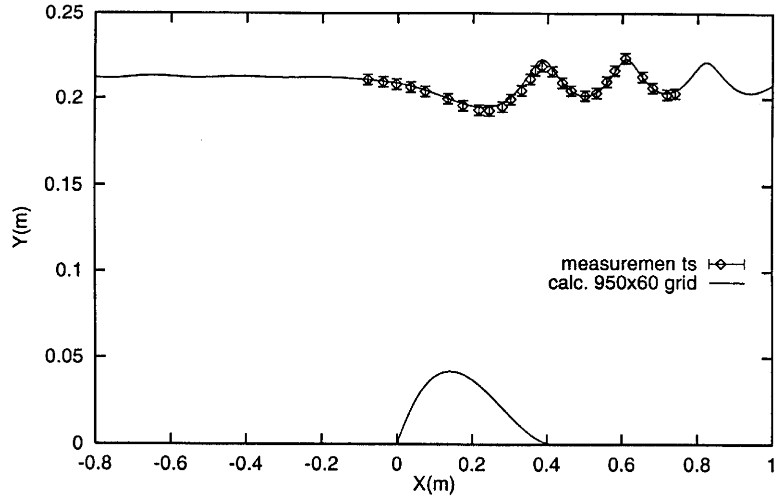

Figure 21. Calculated and measured wave pattern at $Fr = 0{\cdot}43$

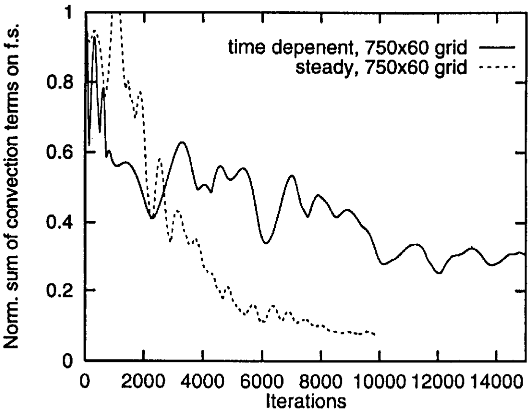

Figure 22. Comparison of convergence rates between steady and time-dependent procedures

mesh sizes the exponential node distribution does not suffer from errors due to the upwind approximation of convection terms. In order to study the influence of the location of the downstream boundary, computations have also been performed for a shorter domain extending up to $x_1 = 1{\cdot}2$ m, while a 600×60 grid was used to obtain equal distances between successive nodes as in previous cases. The comparison of the calculated profiles in Figure 24 shows that there are no significant differences between the two solutions. The contours computed by the 750×60 grids in Figures 23 and 25 as well as the wave amplitudes presented in Table IV are in good agreement with the measured values. The wavelength is underpredicted by almost 6 per cent, a result that was also found by Cahouet,[3] who applied a boundary element method. It should be emphasized here that the experimental uncertainty of the free surface recordings was rather high.

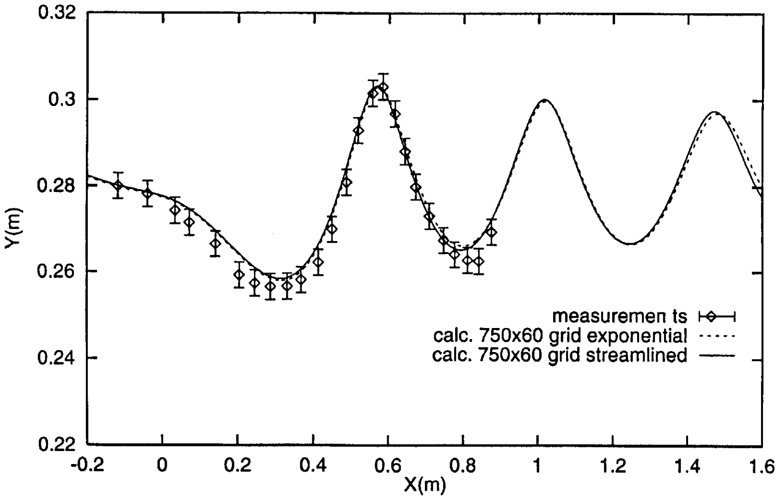

Figure 23. Influence of grid structure on numerical solution

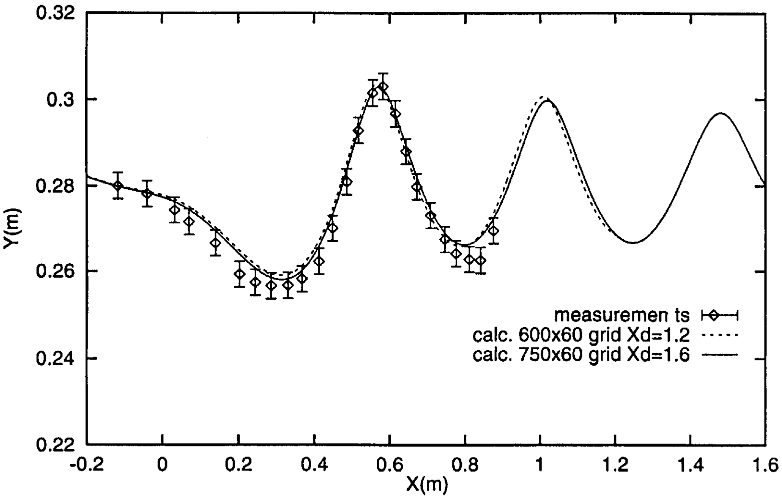

Figure 24. Influence of downstream boundary location on numerical solution

3.2. *Submerged hydrofoil*

The second test case was to study the wave generation above the NACA 0012 hydrofoil, for which extended experiments were carried out by Duncan.[28] Unfortunately, the lift and drag coefficients were not measured in those experiments, and since they are of crucial importance in marine hydrodynamics, calculations were first compared with wind tunnel data for a similar hydrofoil ('unbounded' domain). The case of 8° incidence at $Re = 7{\cdot}5 \times 10^6$ was examined. Calculations were performed in a rectangular domain using a 500×100 grid with 200 pooints on the foil surface. The upstream, downstream, north and south boundaries were at a distance of two chord lengths from the leading edge, the trailing edge and the upper and lower foil surface respectively. When the flow was treated as fully turbulent, the calculated lift and drag coefficients were found as $C_{\mathrm{L}} = 0{\cdot}8245$ and

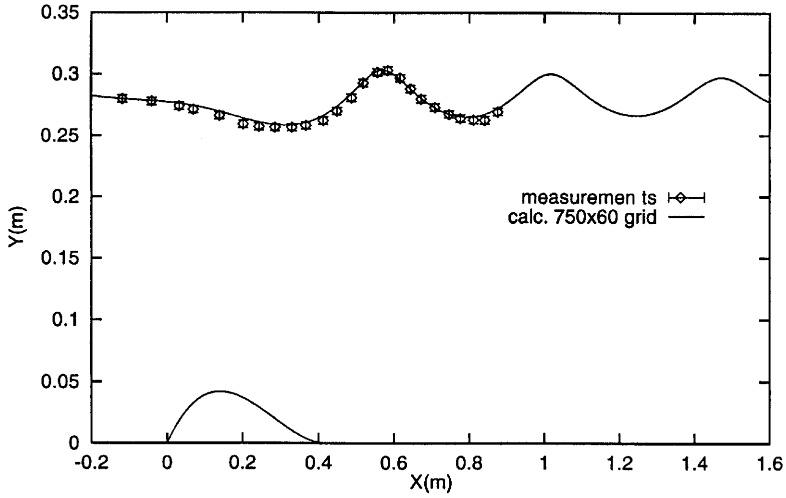

Figure 25. Calculated and measured wave pattern at $Fr = 0{\cdot}52$

Table IV. Comparison between calculated and measured wave characteristics for $Fr = 0{\cdot}52$

	Wavelength (m)	First wave amplitude $2A$ (m)	Second wave amplitude $2A$ (m)
Measured	$0{\cdot}53 \pm 0{\cdot}03$	$0{\cdot}044 \pm 0{\cdot}007$	$0{\cdot}030 \pm 0{\cdot}003$
Calculated	$0{\cdot}47 \pm 0{\cdot}01$	$0{\cdot}045 \pm 0{\cdot}001$	$0{\cdot}033 \pm 0{\cdot}001$

$C_D = 0{\cdot}0279$. Although C_L is in very good agreement with the value of 0·82 measured by Michos *et al.*,[29] the calculated C_D is rather high with respect to the experimental value of 0·023. To investigate the influence of transition which might be a possible reason for this discrepancy, a laminar flow regime was assumed up to specified transition points on the suction and pressure sides of the hydrofoil. These points were calculated by applying the relevant empirical diagrams of Shlichting[30] in conjunction with the laminar boundary layer method of Polhausen.[30] According to this simplified approach, the transition point was estimated to be at $0{\cdot}1c$ from the leading edge on the upper (suction) side and at $0{\cdot}95c$ on the lower side, where c is the chord length. Calculations were performed assuming the flow completely turbulent after these points. Then the drag coefficient was found equal to 0·0238 and the lift coefficient changed to 0·8358, i.e. quite close to the measured values. The satisfactory agreement between computations and measurements is also shown in Figure 26, where the pressure coefficients are compared.

Free surface calculations were performed for the incidence angle of 5° at a nominal upstream velocity U_o of 0·80 m s^{-1}. The foil had a chord of 0·203 m, it was placed at a height of 0·170 m above the tank bottom and its depth of submergence was equal to 0·193 m, resulting in $Fr = 0{\cdot}58$. Based on the chord length, the calculated Reynolds number was $1{\cdot}41 \times 10^5$, implying that the flow was probably transitional during experiments. In all numerical tests the grid extended from 0 to 1·6 m and the leading edge was located at $x_l = 0{\cdot}6$ m, i.e. three chord lengths downstream of the input boundary. A streamlined grid was created above and below $0{\cdot}3d$, where d denotes the vertical distance on U of the foil nose from the water surface and the bottom respectively. The height of the first free surface cell was equal to 0·003 m and the bottom line was assumed a free boundary where

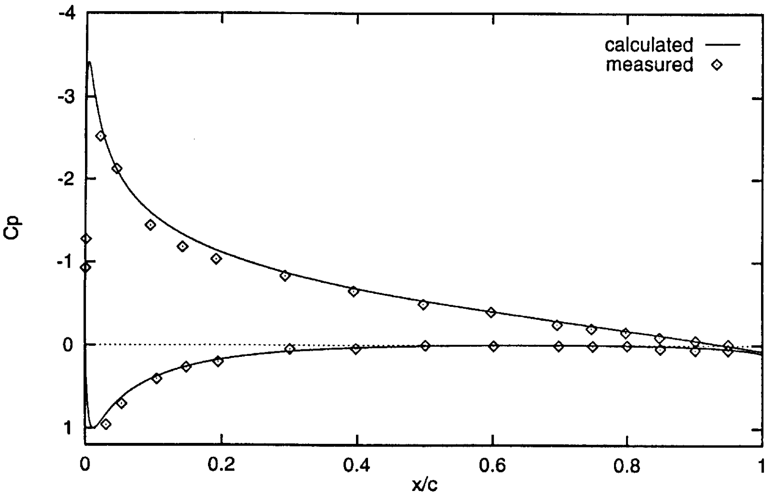

Figure 26. Comparison between calculated and measured C_P-values on foil (8° incidence, $Re = 7{\cdot}5 \times 10^5$)

conditions $u_1 = U_o$ and $u_2 = 0$ applied. In all cases the underrelaxation factors were $ru = 0{\cdot}5$, $rp = 0{\cdot}3$ and $rv = 0{\cdot}5$, while the parameters $IP = 3 \times 15$, $IR = 4$ and $IC = 1$ were adopted in the pressure correction equation.

The steady state equations in conjunction with the quasi-Lagrangian correction (24) were solved to calculate the free surface contour, using 10 internal steps for a specified geometry. To obtain accurate results with the H-type mesh employed, a very fine grid discretization was required in the x_1-direction around the nose of the hydrofoil. Since the time step of the iterative method followed depends on the grid spacing, a high concentration of nodes results in very low time steps and therefore increases considerably the number of iterations. To overcome this shortcoming, the free surface calculation was based on equally spaced points which were corrected according to (24), where the velocity components were calculated using linear interpolations. In this procedure, successfully applied to orthogonal curvilinear grids in previous applications,[31] the surface nodes of the basic mesh are determined by a spline interpolation among the aforementioned, equally distributed points. The convergence histories for a coarse and a fine mesh are plotted in Figure 27, where 600 and 1500 points were used respectively to describe the free surface contour. The corresponding time step underrelaxation factors were equal to 0·5 and 0·8. Similar trends are observed as in the previous applications, i.e. the calculations with the coarse grid lead to faster convergence. An interesting trend of convergence history is presented in Figure 28, where the values of the fine-grid-computed free surface elevations (H) at the first two crests and troughs are plotted. Obviously, fluctuations decay at slower rates as the monitoring point moves downstream. The lift and drag coefficients also show an oscillating behaviour of gradually reduced amplitude (Figure 29), while the momentum and mass residuals (34) reduce as the free surface converges (Figure 30).

Calculated free surface contours using different grid densities of 550 × 60, 550 × 100, 750 × 100 and 950 × 100 nodes are compared with measured values in Figure 31. While the computed contours are in satisfactory agreement with experimental results between the first and the second wave trough, the finest grid in the longitudinal direction predicts more accurately the second wave amplitude. The corresponding y^+-values on the centres of the adjacent-to-the-wall cells were about 20. To investigate the influence of the wall function approximation as well as the existence of laminar regions, two more runs were made with the finest grid of 950 × 100 nodes. In the first case the cell heights close to the foil contour were increased, resulting in values of $y^+ \approx 40$. In the second case, transition points located at 0·45c on the upper and 0·98c on the lower side were calculated according to the previously referred method and the flow was treated as laminar up to them. The calculated wave profiles are

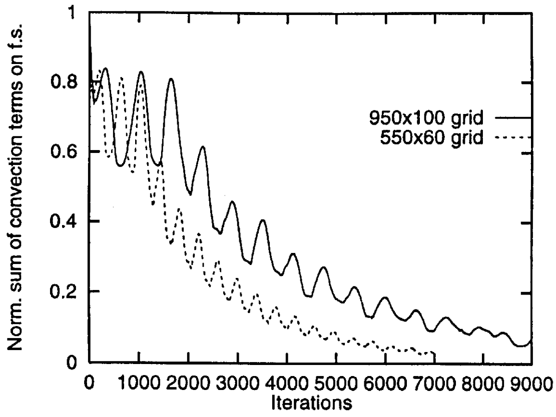

Figure 27. Convergence rates using different grid densities

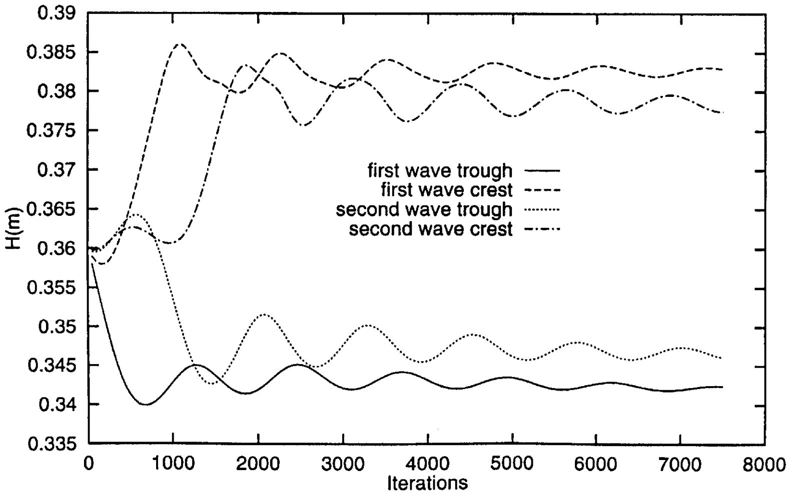

Figure 28. Convergence histories of characteristic free surface points

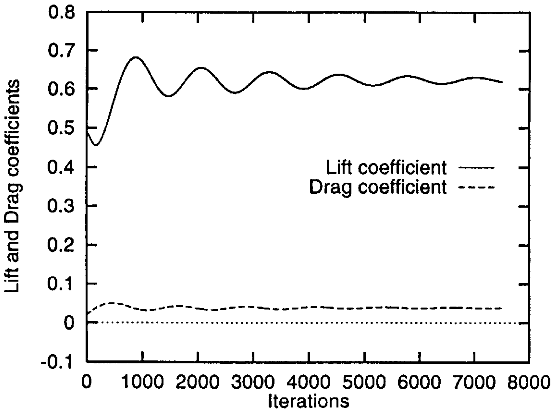

Figure 29. Convergence histories of lift and drag coefficients

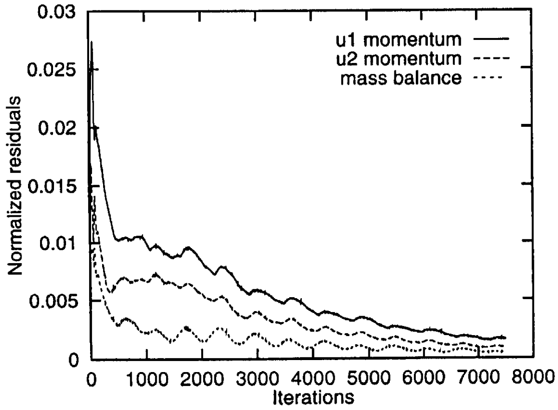

Figure 30. Convergence histories of momentum and mass residuals

presented in Figure 32. While the different y^+-values do not affect significantly the computed wave, the existence of extended laminar flow regimes produce a higher wave amplitude around the first crest. It must be mentioned here that the estimation of the transition points was based on the unbounded flow around the foil, while taking into account the pressure distribution under the free surface, these points should move towards the leading edge. Therefore the first wave crest should lie between the fully turbulent and the transitional flow calculations. Calculated values for the wavelength and the trough-to-crest amplitude $2A$ are compared with measured ones in Table V, while the general view of the generated wave is presented in Figure 33. The numerical results correspond to the fully turbulent computations with the 950×100 grid and underpredict the wavelength by almost 7 per cent and the wave amplitude by 5 per cent. These differences may be related either to numerical approximations (e.g. discretization, restricted computational domain, turbulence model) or to the physics of the particular case, which is transitional, nearly critical and highly unstable.

Finally the calculated lift, drag and skin friction coefficients for all compupted cases are presented in Table VI. An important conclusion can be drawn, namely that the C_L- and C_D-values in the fully turbulent calculations do not differ significantly between the coarse (550×60) and the fine (950×100) grid and consequently the calculation of hydrodynamic forces requires rather acceptable grid resolutions. The tested y^+ ranges do not affect practically the calculated results, while the existence of laminar regions increases C_L by almost 4 per cent and decreases C_D by 6 per cent. The latter decrease is due to the reduction of C_F by 50 per cent, while the pressure component appears higher. Fully turbulent computations were also carried out for the unbounded flow around the hydrofoil at the same Reynolds number and angle of incidence. A grid of 500×100 nodes was used and the calculated coefficients were $C_L = 0{\cdot}5159$, $C_D = 0{\cdot}02356$ and $C_F = 0{\cdot}01014$. Comparing these values with the corresponding ones of Table VI, it is found that the presence of the free surface increases C_L by 18 per cent and C_D by almost 40 per cent, indicating that the generated waves require remarkably higher power to attain the same speed. These differences are mostly due to the drastic changes in the pressure field, as the local C_P plots demonstrate in Figure 34.

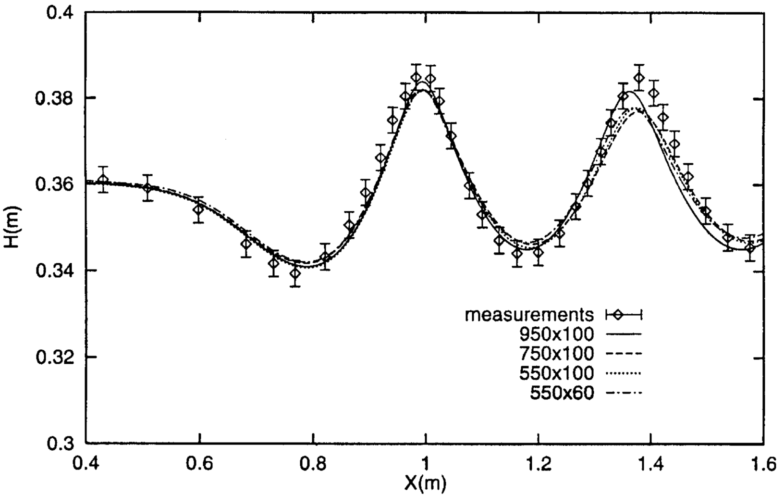

Figure 31. Grid dependence tests and comparison with measurements for submerged hydrofoil ($Re = 1{\cdot}41 \times 10^5$, $Fr = 0{\cdot}58$)

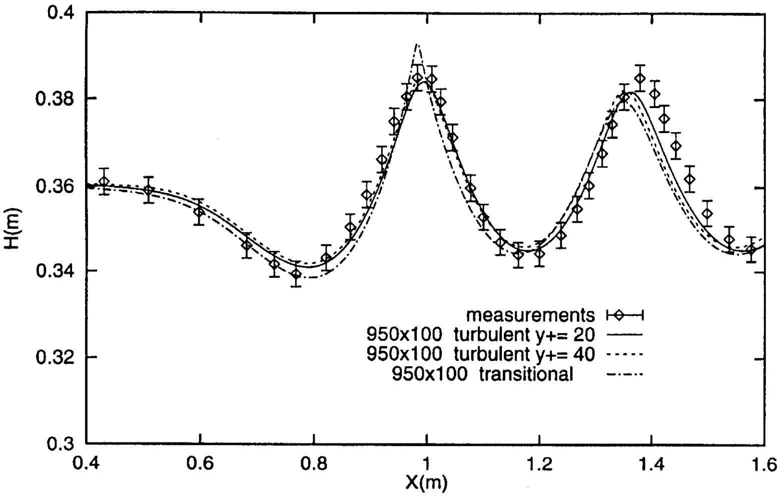

Figure 32. Influence of near-wall grid clustering and transition on calculated free surface

Table V. Comparison between calculated and measured characteristics of wave above hydrofoil

	Wavelength (m)	Wave amplitude 2A (m)
Measured	0·418 ± 0·003	0·042 ± 0·003
Calculated	0·385 ± 0·001	0·040 ± 0·002

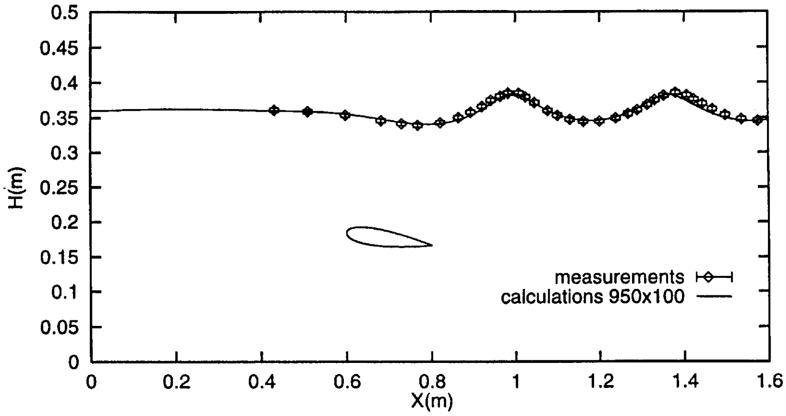

Figure 33. Calculated and measured wave pattern above hydrofoil ($Re = 1{\cdot}41 \times 10^5$, $Fr = 0{\cdot}58$)

Table VI. Calculated lift, drag and skin friction coefficients for submerged hydrofoil

Flow	y^+	Grid ($NI \times NJ$)	C_L	C_D	C_F
Turbulent	40	950 × 100	0·6248	0·0387	0·0112
Transitional	8–20	950 × 100	0·6564	0·0364	0·0064
Turbulent	20	950 × 100	0·6284	0·0385	0·0118
Turbulent	20	750 × 100	0·6267	0·0380	0·0119
Turbulent	20	550 × 100	0·6286	0·0397	0·0120
Turbulent	20	550 × 60	0·6197	0·0404	0·0118

4. CONCLUDING REMARKS

The calculations which have been performed in the present study have shown in general that the predicted free surface characteristics are in satisfactory agreement with the measured data.

Computations of the flow about a bottom topography have shown that the numerical results were influenced by the approximation of convective terms (grid structure) as well as the downstream boundary conditions at low Froude numbers. Applying the adopted Lagrangian method, it was found that convergence depends on the Froude number, the grid size and the free surface underrelaxation. The steady state procedure presented remarkably higher convergence rates than time-dependent calculations, which, in addition, produced unstable results at the critical Froude number. Grid dependence tests revealed that high grid resolutions are required in the longitudinal direction to avoid the problem of wave height numerical decay.

The free surface calculations around the tested hydrofoil presented similar convergence trends with respect to the grid size, i.e. the convergence rate was higher on coarse grids. Although grid dependence tests demonstrated that very fine grids are required to predict accurately the wave height, the calculated lift and drag coefficients were found to be practically insensitive to the grid size in fully turbulent computations. In contrast, the calculated results of both wave height and integrated force coefficients were affected when transition was taken into account.

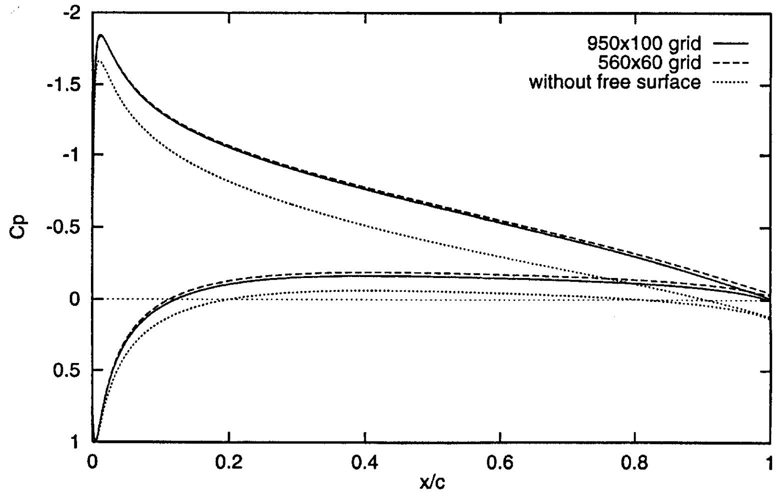

Figure 34. Calculated C_P distributions on foil surface with and without free surface

ACKNOWLEDGEMENT

The author wishes to acknowledge the significant support of the High Performance Computing Center of the NTUA.

REFERENCES

1. J. V. Soulis, 'A numerical method for subcritical and supercritical open channel flow calculation', *Int. j. numer. methods fluids*, **13**, 437–464 (1991).
2. *Proc. CFD Workshop*, Tokyo, 1994, Ship Research Institute, Tokyo, 1994.
3. J. Cahouet, 'Etude numerique et experimentale du probleme bidimensionel de la resistance de vagues non-lineaire', *Ph.D. Thesis*, ENSTA, Paris, 1984.
4. E. Campana, F. Lalli and U. Bulgarelli, 'A boundary element method for a non-linear free surface problem', *Int. j. numer. methods fluids*, **9**, 1195–1206 (1989).
5. G. A. Athanassoulis, S. G. Voutsinas and A. A. Theodoulidis, 'A Hamiltonian principle for steady, nonlinear, free surface flows', *Proc. 1st SIAM Int. Conf. oon Mathematical and Numerical Aspects of Wave Propagation Phenomena*, Strasbourg, 1991, SIAM, Philadelphia, PA, 1991, pp. 387–396.
6. A. A. Theodoulidis, 'Contribution to the study of the steady problem of the perturbed uniform flow with free surface. Linear and nonlinear problem', *Ph.D. Thesis*, NTUA, Athens, 1995 (in Greek).
7. R. M. Coleman, 'Nonlinear calculation of breaking and non-breaking waves behind a two-dimensional hydrofoil', *Proc. 16th ONR Conf.*, 1986, pp. 15.1–15.12.
8. T. Hino, L. Martinelli and A. Jameson, 'A finite volume method with unstructured grid for free surface flow computations', *Proc. 6th Int. Conf. on Numerical Ship Hydrodynamics*, Iowa, 1993, pp. 4.18–4.37.
9. K. J. Kang, 'Numerical simulation of nonlinear waves about a submerged hydrofoil', *Proc. 11th Workshop on Water Waves and Floating Bodies*, Hamburg, 1995, pp. 10.1–10.4.
10. T. Kawamura, H. Kawasima, H. Miyata and Y. Tsuchiya, 'CFD simulation of the flow around planing craft and tandem hydrofoils', *Proc. FAST '95 Conf.*, Hamburg, 1995, pp. 1181–1192.
11. S. Muzaferja, M. Peric and S. D. Yoo, 'Numerische Berechnung der Stroemung um einen Tragfluegel unter freier Oberflaeche', *STG- Sprechtag Numerische Schiffshydrodynamik*, Postsdam, 1995, pp. 5.1–5.10.
12. A. Lungu and K. Mori, 'Developments of the finite difference schemes for free-surface flow computation', *Proc. CFD Workshop*, Tokyo, 1994, Ship Research Institute, Tokyo, 1994, pp. 331–358.
13. H. Liu and M. Ikehata, 'Computation of free surface waves around an arbitrary body by a N–S solver using the pseudocompressibility technique', *Int. j. numer. methods fluids*, **19**, 395–413 (1994).
14. B. E. Launder and D. B. Spalding, 'The numerical computation of turbulent flows', *Comput. Methods Appl. Mech. Eng.*, **3**, 269– 289 (1974).
15. A. D. Gosman and K. Y. M. Lai, 'Finite difference approximations for the transport and Navier–Stokes equations', *Rep. FS/82/18*, Imperial College of Science and Technology, London, 1982, pp. 1–35.
16. I. Demirdzic and M. Peric, 'Finite volume method for prediction of fluid flow in arbitrarily shaped domains with moving boundaries', *Int. j. numer. methods fluids*, **10**, 771–790 (1990).
17. J. H. Ferziger and M. Peric, 'Computational Methods for Fluid Dynamics, Springer, Berlin, 1996.
18. C. Truesdell and R. A. Toupin, *Handbuch der Physik*, Vol. III-1, *The Classical Field Theories*, Springer, Berlin, 1960.
19. G. Jin and M. Braza, 'A non-reflecting outlet boundary condition for incompressible unsteady Navier–Stokes calculations', *J. Comput. Phys.*, **107**, 239–253 (1993).
20. Y. Ventikos, G. Tzabiras and M. Braza, 'Identification of aperiodicity of a Navier–Stokes solution around an aerofoil with dynamical system theory tools', *Proc. 5th Int. Symp. on Refined Flow Modeling and Turbulence Measurements*, Paris, 1993, pp. 793–800.
21. J. Farmer, L. Martinelli and A. Jameson, 'A fast multigrid method for solving the nonlinear ship wave problem with a free surface', *Proc. 6th Int. Conf. on Numerical Ship Hydrodynamics*, Iowa, 1993, pp. 4.1–4.17.
22. S. V. Patankar and D. B. Spalding, 'A calculation procedure for heat, mass and momentum transfer in 3-D parabolic flows', *Int. J. Heat Mass Transfer*, **15**, 1787–1806 (1972).
23. J. P. Doormal and G. D. Raithby, 'Enhancements of the SIMPLE method for predicting incompressible fluid flows', *J. Comput. Phys.*, **88**, 305–336 (1990).
24. P. J. Roache, *Computational Fluid Dynamics*, Hermosa, Albuquerque, NM, 1972.
25. G. D. Tzabiras, 'A numerical investigation of the Reynolds scale effect on the resistance of bodies of revolution', *Ship Technol. Res.*, **39**, 28–44 (1992).
26. G. D. Tzabiras, 'Resistance and self-propulsion numerical experiments on two tankers at model and full scale', *Ship Technol. Res.*, **40**, 20–38 (1993).
27. B. Alessandrini and G. Delhommeau, 'Simulation of three-dimensional unsteady viscous free surface flow around a ship model', *Int. j. numer. methods fluids*, **19**, 321–342 (1994).
28. J. H. Duncan, 'The breaking and non-breaking wave resistance of a two-dimensional hydrofoil', *J. Fluid Mech.*, **126**, 507–520 (1983).

29. A. Michos, G. Bergeles and N. Athanassiadis, 'Aerodynamic characteristics of NACA 0012 aerofoil in relation to wind generators', *Wind Eng.*, **7**, 247–261 (1983).
30. H. Schlichting, *Boundary Layer Theory*, McGraw-Hill, New York, 1968.
31. G. Tzabiras and Y. Ventikos, 'Calculation of the wave pattern generated by a 2D submerged hydrofoil: a Navier–Stokes approach', *Proc. 1st SIAM Int. Conf. on Mathematical and Numerical Aspects of Wave Propagation Phenomena*, Strasbourg, 1991, SIAM, Philadelphia, PA, 1991, pp. 406–414.